AGU PUBLICATIONS

Geophysical Research Letters

RESEARCH LETTER
10.1002/2016GL071225

Key Points:
- Iron-rich (Mg,Fe)O may be an important component of ultralow-velocity zones at the base of the lower mantle
- Compositional dependence of sound velocities of iron-rich (Mg,Fe)O was measured as a function of pressure
- Using this work, seismic observations of ultralow-velocity zones can be interpreted in the context of local iron enrichment

Correspondence to:
J. K. Wicks,
jwicks@princeton.edu

Citation:
Wicks, J. K., J. M. Jackson, W. Sturhahn, and D. Zhang (2017), Sound velocity and density of magnesiowüstites: Implications for ultralow-velocity zone topography, *Geophys. Res. Lett.*, *44*, doi:10.1002/2016GL071225

Received 15 SEP 2016
Accepted 31 JAN 2017
Accepted article online 2 FEB 2017

Sound velocity and density of magnesiowüstites: Implications for ultralow-velocity zone topography

June K. Wicks[1,2], Jennifer M. Jackson[1], Wolfgang Sturhahn[1], and Dongzhou Zhang[1,3]

[1]Division of Geological and Planetary Sciences, California Institute of Technology, Pasadena, California, USA, [2]Department of Geosciences, Princeton University, Princeton, New Jersey, USA, [3]Hawai'i Institute of Geophysics and Planetology, University of Hawai'i at Manoa, Honolulu, Hawaii, USA

Abstract We explore the effect of Mg/Fe substitution on the sound velocities of iron-rich $(Mg_{1-x}Fe_x)O$, where $x = 0.84$, 0.94, and 1.0. Sound velocities were determined using nuclear resonance inelastic X-ray scattering as a function of pressure, approaching those of the lowermost mantle. The systematics of cation substitution in the Fe-rich limit has the potential to play an important role in the interpretation of seismic observations of the core-mantle boundary. By determining a relationship between sound velocity, density, and composition of (Mg,Fe)O, this study explores the potential constraints on ultralow-velocity zones at the core-mantle boundary.

1. Introduction

Ultralow-velocity zones (ULVZs) are typically small (10–100 km high) structures at the base of Earth's mantle that are characterized by unusually low seismic velocities: ~5–20% drop in compressional sound velocities V_P and ~5–30% drop in shear sound velocities V_S. Such significantly reduced sound velocities have been shown to be attributable to either the existence of partial melt [*Williams and Garnero*, 1996] or local iron enrichment [*Knittle and Jeanloz*, 1991; *Wicks et al.*, 2010; *Rost et al.*, 2013].

Recent seismic observations of the core-mantle boundary have expanded both the number and variability of ULVZ observations, including a very large ULVZ [*Cottaar and Romanowicz*, 2012] to areas on the core-mantle boundary with moderate velocity drops, so called "rolling hills" [*Sun et al.*, 2013]. Combined with previous work, details such as interior fine-scale structure [*Rost et al.*, 2006], aspect ratio [*Wen and Helmberger*, 1998a], and interface concavity [*Helmberger et al.*, 2000] paint an increasingly diverse and complicated picture of the lowermost mantle. The wide variety in ULVZ character and further complexity at the core-mantle boundary permit an equally diverse set of mineralogical conditions and could reflect large amounts of heterogeneity in chemistry (such as Fe enrichment, Si depletion), mineralogy (presence of postperovskite, hydrated minerals), and phase (solid, partial melt).

A partial melting hypothesis for ULVZs takes advantage of the ease of reducing bulk and shear moduli by mixing with liquid [*Berryman*, 2000]. It also implies a special circumstance: an intersection of the mantle geotherm with the mantle solidus at a location just a few kilometers above the core-mantle boundary, which may be true for very iron rich [*Pradhan et al.*, 2015; *Kato et al.*, 2016] and hydrated alkalic [*Nomura et al.*, 2014] systems. Dynamic models have found that the amount of liquid required to reduce sound velocities to such an extent would interconnect and drain to the lowermost 1 km of mantle [*Hernlund and Tackley*, 2007], but could remain several kilometers above the core-mantle boundary if vigorously stirred [*Hernlund and Jellinek*, 2010]. Alternatively, 3-D models suggest that sufficient liquid pinning on grain boundaries is plausible [*Wimert and Hier-Majumder*, 2012], and subsequent melt compaction could explain the observed inverted velocity structure [*Hier-Majumder*, 2014].

More accurate mineral physics measurements allow us to extend the interpretations of ULVZs one step further. For example, *Thomas and Asimow* [2013] measured the equation of state of silicate liquids to describe the evolution of a crystallizing magma ocean and found that partial melt residues of *ambient mantle* composition would not be gravitationally stable unless combined with another denser solid. If such ULVZs exist, then inferences could be drawn about isolated chemical reservoirs in the mantle.

Sound velocity measurements of iron-enriched mantle minerals have found that partial melting is not required to produce the characteristic low sound velocities of ULVZs [*Mao et al.*, 2006; *Wicks et al.*, 2010]. As a result, this heterogeneity observed at the core-mantle boundary could represent a chemical signature rather than a phase change. Follow-up dynamic models explored the constraints given by sound velocities and density anomalies of a solid ULVZ [*Bower et al.*, 2011]. It was found that an iron-rich assemblage of (Mg,Fe)O and bridgmanite or of iron-rich (Mg,Fe)O with a surrounding mantle of average composition could easily reproduce the range of both sound velocities and topography of ULVZs detected by seismic studies with reasonable volume fractions of (Mg,Fe)O.

Here we expand on previous work and present sound velocity systematics of iron-rich (Mg,Fe)O from experiments using Nuclear Resonant Inelastic X-ray Scattering (NRIXS) of $(Mg_{0.06}Fe_{0.94})O$ and FeO. In addition to providing insight into the compositional dependence of sound velocities, this paper also highlights improvements in the methodology since the publication of the previous work [*Wicks et al.*, 2010]. Most notably, availability of in situ X-ray diffraction permits direct measurements of the sample's unit cell volume and thus provides in situ density (ρ) of our sample for the NRIXS measurements. Together with a reliable equation of state for this material [*Wicks et al.*, 2015], we report the Debye sound velocities as a function of density and pressure.

2. Experimental Methods

$(Mg_{0.058(1)}Fe_{0.942(1)})O$ (Mw94) and $Fe_{0.941(2)}O$ (FeO, wüstite) samples were synthesized at ambient pressure using 95% enriched ^{57}Fe (previously described in *Chen et al.* [2012] and *Wicks et al.* [2015]). The chemical composition of wüstite was computed based upon its lattice parameter ($a = 4.306(1)$ Å) and the relationship reported in *McCammon and Liu* [1984]: $a = 3.856 + 0.478x$ for Fe_xO. High pressure was achieved using 400 μm-culet anvils and 300 μm-culet/370 μm-beveled anvils in panoramic diamond anvil cells (DACs). These panoramic DACs have three radial openings that provide access to inelastically scattered photons using avalanche photodiode detectors and a 90° downstream opening angle for in situ X-ray diffraction. The cells prepared with Mw94 had a c-BN seat on the downstream side that permitted in situ X-ray diffraction measurements with NRIXS measurements.

A low-pressure data point (11.1 GPa) was taken of Mw94 in a DAC with a KCl pressure-transmitting medium and a beryllium gasket. At higher pressures, samples were supported by a boron epoxy insert and pressure-transmitting medium in a beryllium sample gasket with rubies on either side, one on each culet. Ambient pressure measurements were conducted in air.

Nuclear resonance scattering experiments were conducted at Sector 3-ID-B of the Advanced Photon Source (APS) at Argonne National Laboratory. The storage ring was operated in low-emittance top-up mode with 24 bunches separated by 153 ns. In these experiments, X-rays are monochromatized to 1 meV bandwidth [*Toellner*, 2000], scanned around the nuclear resonance energy of 14.4125 keV, and focused to $10 \times 11 \mu m^2$ [*Zhang et al.*, 2016] on an ^{57}Fe-containing sample. The delayed emission of nuclear resonant fluorescence radiation into a large solid angle is observed using avalanche photodiode detectors [*Sturhahn and Jackson*, 2007]. Energy scans were collected over a minimum energy range of $-60 \rightarrow +70$ meV, although most scans were collected up to 80 meV. At the highest compression point of Mw94 (~85 GPa) and FeO (~96 GPa), an extended energy range scan was conducted to capture the weak contributions to the vibrational spectrum at around 80 meV.

During the Mw94 measurements, a MAR345 image plate inserted downstream from the sample was used to record the X-ray diffraction pattern of the sample in situ. The angle-dispersive X-ray pattern was integrated radially using the Fit2D software [*Hammersley et al.*, 1996] to determine unit cell volumes and pressures via the equation of state of Mw94 [*Wicks et al.*, 2015]. A CeO_2 standard was used to calibrate both the X-ray beam center and the distance between the X-ray focus spot and the detector. The unit cell volumes of FeO were measured at Sector 12.2.2 of the Advanced Light Source (ALS) (ambient pressure) and at Sector 13-ID-D of the APS (high density).

3. Sound Velocities

Nuclear resonant inelastic X-ray scattering (NRIXS) spectra were collected for Mw94 over the pressure range 0 to 85 GPa (0, 92, 96 GPa for FeO) and processed using the PHOENIX software with appropriate uncertainties

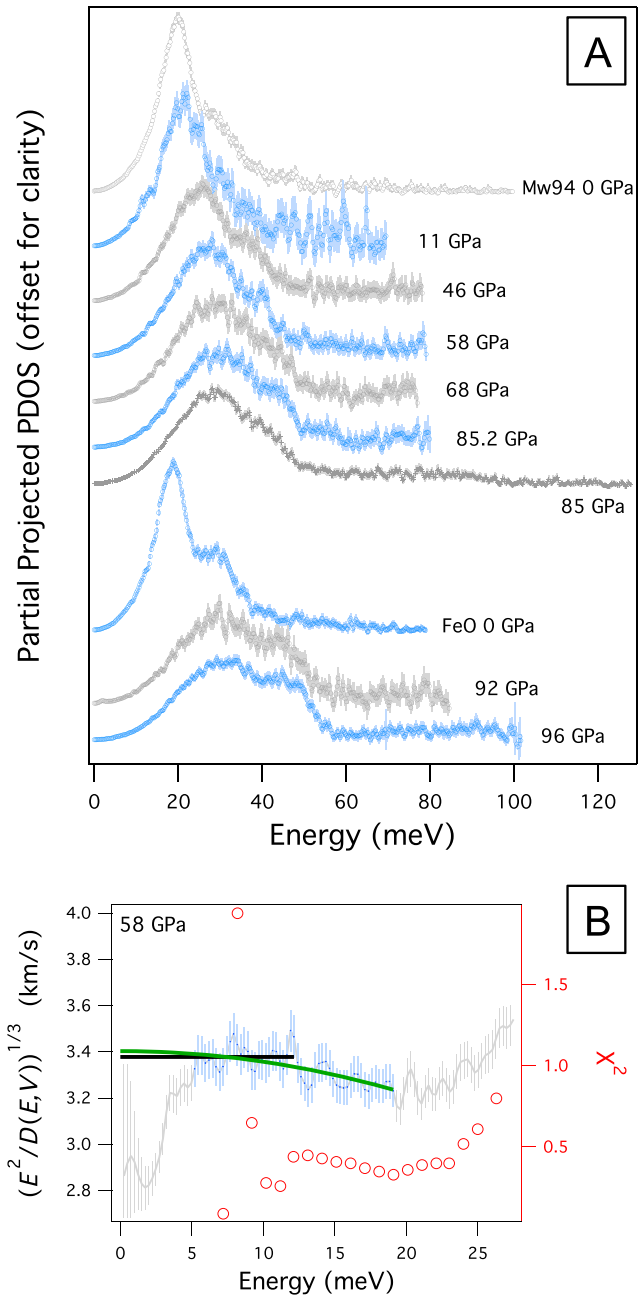

Figure 1. (a) Partial projected phonon density of states of $(Mg_{0.06}Fe_{0.94})O$ at 300 K extracted from raw NRIXS data using PHOENIX [*Sturhahn*, 2000]. Spectra are offset in the *y* direction for clarity. (b) Debye velocity determination using the *psvl* subroutine in PHOENIX at 58 GPa. Green and black lines are V_D (km/s) at $E = 0$ (equation 1). A quadratic fit to $V(E)$ best describes data up to 12 meV (black line). More of the PDOS can be included if an empirical function is instead used (green line), where corresponding χ^2 values (open red circles) calculated in *psvl* for differing energy ranges are plotted at the E_{max} of each calculation (Table 1).

[*Sturhahn*, 2000] using methods described in *Sturhahn* [2004] and W. Sturhahn (NRIXS Software, 2015, www.nrixs.com). In this open-source software, the partial projected phonon density of states (PDOS) pertaining to the ^{57}Fe site is extracted [*Sturhahn and Jackson*, 2007] (Figure 1a).

The Debye sound velocity, V_D, is related to the low-energy region of the PDOS in the following manner:

$$V(E) = \left\{ \frac{m E^2}{2\pi^2 \hbar^3 \rho D(E)} \right\}^{\frac{1}{3}} \quad \text{and} \quad V_D = V(0) \ , \tag{1}$$

where m is the mass of the resonant nucleus, ρ is the mass density of the sample, and $D(E)$ is the PDOS.

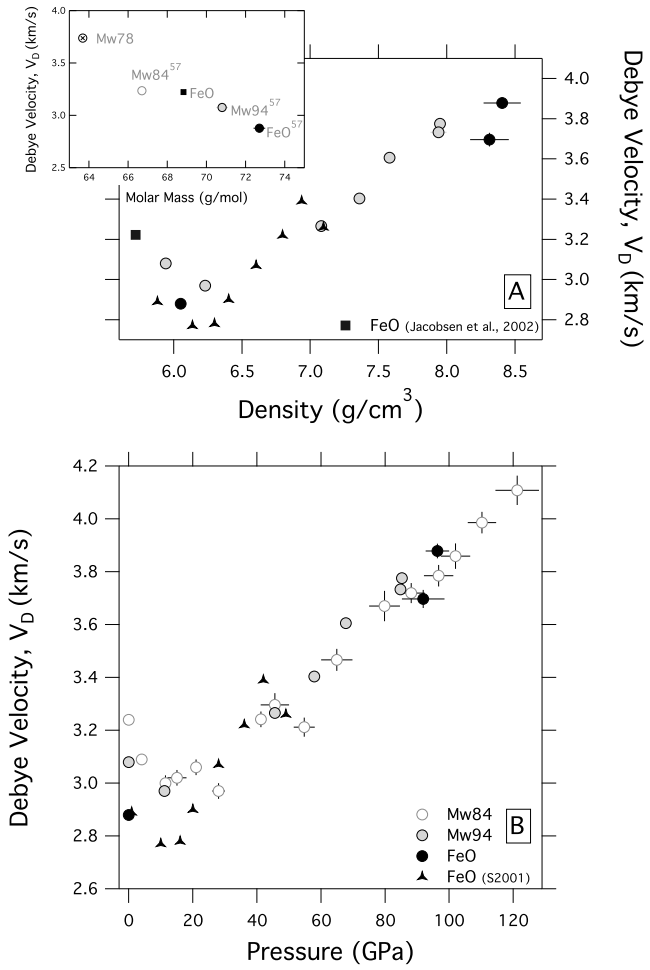

Figure 2. (a) Debye velocity (V_D) of $(Mg_{0.06}Fe_{0.94})O$ compared to FeO as a function of measured density. $(Mg_{0.06}Fe_{0.94})O$ volumes were measured in situ at Sector 3-ID-B of the Advanced Photon Source (APS). (inset) V_D as a function of molar mass in iron-rich (Mg,Fe)O (Mw78 and FeO, using c_{ij}'s reported in *Jacobsen et al.* [2002] and appropriate NRIXS averaging: Mw84[57] [*Wicks et al.*, 2010], Mw94[57] and FeO[57], this study). (b) V_D evolution as a function of pressure. Pressure (for Mw94 and FeO, this study) and density (for Mw84 [*Wicks et al.*, 2010] and FeO (S2001) [*Struzhkin et al.*, 2001]) were calculated using the equation of state of Mw94 [*Wicks et al.*, 2015].

Figure 1b shows, in detail, two different phonon dispersion models applied to the low-energy region of the PDOS to derive the Debye velocity using the *psvl* subroutine in PHOENIX (W. Sturhahn, online report, 2015). In this procedure, the PDOS is scaled according to equation (1). A strict "Debye-like" region varies quadratically with energy corresponding to acoustic phonons with a small wave number (long wavelength), which would be independent of energy in the scaling shown in Figure 1b (black line).

More data can be included if the strict energy-dependent scaling is not imposed, fitting instead an empirical function $f(E) \approx V_D \{1 - (E/E_0)^2\}$ that maintains a Debye-like behavior approaching zero energy (green line, Figure 1b), where E_0 and V_D are optimized in a standard least squares fit procedure in *psvl* [*Jackson et al.*, 2009]. The empirical relation for the dispersion of acoustic phonons often assumes that the phonon energies reach a maximum value at the Brillouin zone boundary. However, this assumption is not necessary, rather the quadratic energy term can be understood as a lowest-order correction [*Sturhahn and Jackson*, 2007].

In either case, the zero-energy limit of the scaled PDOS is the Debye velocity (V_D). The lower energy limit of the fitting region to obtain this intercept depends on the incident X-ray bandwidth and the successful subtraction of the elastic peak, while the upper limit of the fitting region is determined both by the χ^2 of fitting and reasonable energy ranges where the acoustic phonons behave like sound waves [*Sturhahn and Jackson*, 2007].

Table 1. Magnesiowüstite Data[a]

Sample	Volume (Å^3/atom)	Density (g/cc)	Pressure (GPa)	V_D (km/s)	V_P (km/s)	V_S (km/s)	G (GPa)	K_T (GPa)	K_S (GPa)	Energy Range (meV)
FeO[b]	9.979(4)[c]	6.05(3)	0	2.88(1)	6.47(9)	2.538(1)	38.9(3)	197(7)	201(7)	3.2–17.1
	7.3(1)[d]	8.3(1)	92(7)	3.70(3)	7.8(1)	3.27(3)	88.8(1.7)	390(11)	393(11)	4.5–18.8
	7.2(1)[d]	8.4(1)	96(4)	3.88(3)	7.95(8)	3.43(3)	99.1(1.5)	397(8)	400(8)	4.2–19.8
Mw94[e]	9.904(1)	5.94(2)	0	3.08(1)	6.61(9)	2.72(1)	43.8(4)	197(7)	201(7)	5.0–14.1
	9.446(1)[f]	6.23(2)	11.10(2)	2.97(2)	6.80(7)	2.62(2)	42.7(7)	227(6)	230(6)	5.7–19.9
	8.30(2)	7.08(3)	45.6(7)	3.27(2)	7.41(3)	2.88(2)	58.8(8)	307(3)	310(3)	5.7–19.6
	7.99(2)	7.36(4)	57.8(8)	3.40(2)	7.58(3)	3.00(2)	66.4(9)	332(2)	335(2)	5.2–19.1
	7.76(2)	7.58(4)	67.7(8)	3.61(2)	7.75(3)	3.19(2)	76.9(9)	350(2)	353(2)	3.7–20.8
	7.41(2)	7.94(6)	85(1)	3.73(2)	7.92(4)	3.30(2)	86.5(9)	380(4)	382(4)	5.2–17.9
	7.40(1)	7.95(3)	85.2(6)	3.78(2)	7.94(4)	3.34(2)	89(1)	380(4)	383(4)	4.9–21.0
Mw84[g]	9.79(4)	5.7(1)	0	3.24(1)	6.83(8)	2.86(1)	46.8(3)	197(7)	201(7)	3.8–13.8
	9.59(9)	5.8(6)	4.0(3)	3.09(2)	6.83(9)	2.72(2)	42.8(7)	208(6)	212(6)	3.7–17.2
	9.26(9)	6.0(6)	11.4(3)	3.00(3)	6.93(8)	2.65(2)	41.9(7)	228(6)	231(6)	3.5–16.0
	9.1(2)	6.1(1)	15(3)	3.02(3)	7.01(10)	2.67(3)	43(1)	237(5)	240(5)	5.7–16.0
	8.90(8)	6.2(6)	21.0(4)	3.06(3)	7.13(7)	2.70(2)	45.2(8)	252(5)	255(5)	3.8–14.8
	8.7(1)	6.4(9)	28(2)	2.97(3)	7.19(8)	2.62(3)	43.7(8)	268(4)	271(4)	4.7–18.2
	8.3(1)	6.7(8)	41(1)	3.24(3)	7.48(6)	2.86(3)	55(1)	298(3)	301(3)	3.7–17.2
	8.2(2)	6.8(2)	46(4)	3.30(4)	7.55(10)	2.91(4)	57(1)	307(3)	310(3)	3.7–19.7
	7.9(1)	7.0(1)	55(3)	3.21(4)	7.60(8)	2.83(3)	56(1)	326(2)	329(2)	3.7–19.7
	7.7(2)	7.2(2)	65(5)	3.47(4)	7.80(9)	3.06(4)	67(2)	345(2)	348(2)	4.7–20.7
	7.4(1)	7.5(2)	80(5)	3.67(6)	7.99(9)	3.24(5)	79(3)	371(3)	374(3)	4.2–15.2
	7.3(1)	7.7(1)	88(4)	3.72(4)	8.06(9)	3.29(3)	83(2)	384(5)	387(5)	3.7–18.7
	7.1(1)	7.8(2)	97(5)	3.79(4)	8.12(10)	3.35(4)	88(2)	397(6)	400(6)	3.7–16.2
	7.0(1)	7.9(2)	102(5)	3.86(5)	8.18(10)	3.41(4)	93(2)	406(7)	409(7)	3.7–18.7
	6.9(1)	8.1(1)	110(4)	3.99(4)	8.26(10)	3.53(4)	101(2)	416(9)	419(9)	3.7–16.2
	6.8(1)	8.3(2)	121(7)	4.11(6)	8.34(13)	3.64(5)	110(3)	429(11)	432(11)	3.7–16.2

[a]Unless noted otherwise, unit cell volume was measured in situ at Sector 3. Corresponding pressure and the isothermal (K_T) and adiabatic (K_S) bulk moduli were determined using the thermal equation of state of Mw94 ($K_{0T} = 197.4 \pm 6.5$ GPa, $K'_{0T} = 2.79(9)$, $\Theta_D = 426$ K, $\gamma_0 = 1.72(8)$, $q = 0.5$) [*Wicks et al.*, 2015]. V_P and V_S were calculated using K_S. The energy range used to determine the Debye velocities is provided. Number in parenthesis is the error on the last digit.

[b]Composition $Fe_{0.941}O$. Pressure errors at high pressure reflect more information from ex situ measurements: a pressure gradient across the sample probe area and the effect of sample strain on rhombohedral distortion.

[c]Volume was measured at Sector 12.2.2, ALS.

[d]Volume was measured at Sector 13, GSECARS.

[e]Composition ^{57}Fe-enriched $(Mg_{0.058(1)}Fe_{0.942(1)})O$.

[f]Pressure-transmitting medium of KCl rather than B epoxy.

[g]Composition ^{57}Fe-enriched $(Mg_{0.18}Fe_{0.78}Ti_{0.04})O$.

In the inset of Figure 2a, V_D is shown as a function of molar mass in iron-rich (Mg,Fe)O at room pressure. For comparison, the V_D of $(Mg_{0.22}Fe_{0.78})O$ (Mw78) and FeO were numerically determined using an open-source *sound velocities from elastic constants* (svec) routine within the MINeral physics UTility software package, MINUTI (W. Sturhahn, online report, 2015). From C_{ij} elastic moduli reported by *Jacobsen et al.* [2002] using the directionally averaged Christoffel equation [*Sturhahn and Jackson*, 2007], we calculated that V_D (Mw78) = 3.7379 km/s and V_D (FeO) = 3.2225 km/s. These values, combined with measurements in this study of Mw84[57] [*Wicks et al.*, 2010] and Mw94[57] and FeO[57], show a linear decrease in velocity with increasing molar mass, a trend reminiscent of Birch's Law.

Figure 2a shows Debye velocities determined using the density calculated from in situ X-ray diffraction for $(Mg_{0.06}Fe_{0.94})O$ (measured at 3-ID-B). Also shown are sound velocities calculated for FeO using densities determined from ex situ X-ray diffraction.

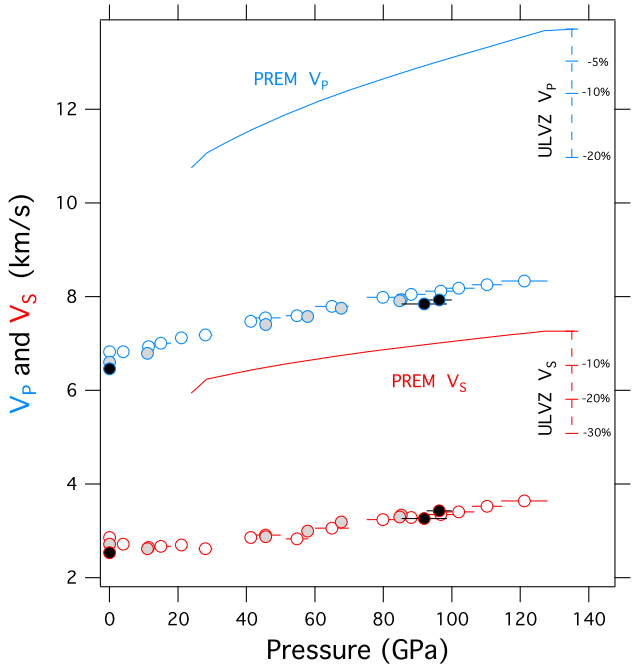

Figure 3. Compressional (V_P, blue) and shear (V_S, red) wave velocities of $(Mg_{0.16}{}^{57}Fe_{0.84})O$ (Mw84, empty circles), $(Mg_{0.06}{}^{57}Fe_{0.94})O$ (Mw94, gray-filled circles), and ^{57}FeO, black-filled circles, all measured at 300 K (Table 1). Errors calculated on velocity are smaller than the symbol size. For comparison, the V_P and V_S of the Preliminary Reference Earth Model, PREM, are shown for lower mantle pressures [*Dziewonski and Anderson*, 1981] and velocity decrements reported for ULVZs (see text for references).

In order to compare with previous NRIXS work where in situ density was not measured and pressure was determined by ruby fluorescence alone [*Struzhkin et al.*, 2001; *Wicks et al.*, 2010], Figure 2b shows measured V_D as a function of pressure. For the sake of comparison, the same equation of state (EOS) parameters was used for all iron-rich compositions, scaled to their ambient pressure initial density. The third-order Birch-Murnaghan/Mie-Grüneisen EOS was measured for Mw94 (K_{0T}197.4 ± 6.5 GPa, $K'_{0T} = 2.79(9)$, $\Theta_D = 426$ K, and $\gamma_0 = 1.72(8)$, $q = 0.5$) [*Wicks et al.*, 2015]. The effect of using the equation of state (and therefore ρ) of FeO [*Fischer et al.*, 2011a] on V_D is negligible compared to the precision of this measurement. For Mw84, on the other hand, using the EOS described above rather than that of $(Mg_{0.22}Fe_{0.78})O$ [*Zhuravlev et al.*, 2010] removed the need for extrapolations of tens of GPa in pressure [*Zhuravlev et al.*, 2010; *Wicks et al.*, 2010].

At low pressures, all studies exhibit the initial sound velocity softening with increasing pressure characteristic of iron-rich (Mg,Fe)O associated with the magnetic ordering transition at ~15–30 GPa, dependent on composition [*Struzhkin et al.*, 2001; *Jacobsen et al.*, 2002; *Wicks et al.*, 2010]. Interestingly, at pressures above this transition, the Debye velocities as a function of composition are almost indistinguishable.

For an isotropic solid, V_D is related to the seismically relevant aggregate compressional (V_P) and shear (V_S) velocities by

$$\frac{3}{V_D^3} = \frac{1}{V_P^3} + \frac{2}{V_S^3} \tag{2}$$

$$\frac{K_S}{\rho} = V_P^2 - \frac{4}{3}V_S^2 = V_\phi^2 \tag{3}$$

where K_S is the adiabatic bulk modulus, ρ is the density, and V_ϕ is the bulk sound velocity. K_S is related to the isothermal bulk modulus, K_T, by $K_S = K_T(1 + \alpha\gamma T)$ with temperature T, thermal volume expansion coefficient α, and Grüneisen parameter γ.

The seismically relevant V_P and V_S were calculated from V_D and values of K_S, α, γ, and ρ mentioned above [*Wicks et al.*, 2015]. The results are summarized in Table 1. In Figure 3a, we plot V_P and V_S as a function of pressure.

4. Discussion

As discussed previously [*Sturhahn and Jackson*, 2007], the choice of equation of state significantly affects the value of compressional wave velocity. Using in situ X-ray diffraction, the Debye sound velocity is determined independent of an equation of state, but calculation of the seismically relevant V_P and V_S requires an independent determination of the adiabatic bulk modulus. To explore the effect of equation of state choice on the calculated V_P, which can be shown from equations 2 and 3 to be most sensitive to V_ϕ, we calculate the V_P of FeO using the equation of state of FeO from *Fischer et al.* [2011a] and compare it to that calculated from the equation of state of Mw94 [*Wicks et al.*, 2015]. We find that the compressional velocities at the highest pressure would be higher by 0.5 km/s, rendering it indistinguishable from the other compositions.

Determination of adiabatic bulk modulus is given by the thermal equation of state of Mw94 [*Wicks et al.*, 2015]. At the highest pressure point of 85.2 GPa, for example, sound velocity determinations using K_S rather than K_T resulted in a V_P increase of 0.3% and a V_S decrease of 0.03%. As such, we used K_S for all calculations of V_P and V_S published here.

The cubic to rhombohedral transition of iron-rich (Mg,Fe)O has been shown through this and previous work to be preceded by shear modulus "softening" as a function of pressure, while it has been showed experimentally that the bulk modulus remains unaffected [*Zhuravlev et al.*, 2010; *Wicks et al.*, 2015]. The effect of temperature on the compressional and shear velocities of magnesiowüstite at high pressure is not yet known; therefore, the consequences of the high temperature rhombohedral to cubic phase boundary and coupling with Fe magnetic transitions are not known and thus the effect on the sound velocities is not clear.

The rhombohedral distortion transition has been shown to be sensitive to deviatoric stress [*Shu et al.*, 1998]. Comparison of both in situ and ex situ X-ray diffraction patterns of Mw94 at high pressure with the temperature-annealed equation of state of the same material in a Ne pressure-transmitting medium confirms the lesser degree of distortion in a strained environment. The in situ X-ray diffraction measurement of the 200 (cubic) = 012 (rhombohedral) peak was used to calculate unit cell volume, with an estimate of error due to strain bracketed by no distortion (i.e., cubic) and ideal distortion ($c/a = 2.457 + .003P$) [*Wicks et al.*, 2015]. As pressure was determined only by one reflection, limited by the X-ray energy and bandwidth, we conclude that the error bar calculated by considering rhombohedral distortion is a lower bound. In contrast, the ex situ measurements of FeO, which reflect both sample strain and pressure/stress gradient across the NRIXS-probed sample, likely represent an upper bound on pressure uncertainty, allowing us to conclude that a reasonable pressure error on Mw94 is 4–5 GPa. We note that within scatter, the measurement utilizing a KCl pressure medium is consistent with trends of the other measured velocities.

5. Geophysical Implications

When comparing the sound velocities determined in this study at 300 K to the Preliminary Reference Earth Model (PREM) [*Dziewonski and Anderson*, 1981], a 1-D model for Earth properties, it is clear that the values for iron-rich (Mg,Fe)O are much lower than those of ambient mantle and lower than those of ultralow-velocity zones (Figure 3a). It is very reasonable, then, to hypothesize that ultralow velocities can be explained by either a physical mixture of iron-rich oxide with ambient mantle or by an equilibrium assemblage of iron-rich mantle materials.

In *Bower et al.* [2011], the stability of solid ULVZs was explored using geodynamic simulations, which gave insight into the relationship between relative density anomaly and ULVZ shape. This work places an external constraint on ULVZ density for seismic observations that model the full waveform using 2-D or 3-D topography [*Wen and Helmberger*, 1998b; *Helmberger et al.*, 1998; *Sun et al.*, 2013]. When combined with the relationship between density (e.g., via iron enrichment) and sound velocity of materials, ULVZ interpretations can be taken one step further—individual observations can be modeled as simplified assemblages of phases (e.g., (Mg,Fe)O + (Mg,Fe)SiO_3) and compared to other ULVZs to estimate lateral chemical heterogeneity.

With our measurements, we can begin to explore the relationship between sound velocity and iron content of an assemblage. To model the sound velocities of iron-rich (Mg,Fe)O at the core-mantle boundary, the Debye sound velocities in Figure 2b were extrapolated to 135 GPa (V_D=4.27(21) km/s), V_P and V_S were calculated for Mw84 and Mw94, after adjusting density for the natural iron enrichment. There are no reports of the cross $P-T$ derivatives for V_P and V_S of iron-rich (Mg,Fe)O. Therefore, we use the derivatives reported for MgO under these PT conditions. We applied a temperature dependence of $\delta V_P/\delta T = -8.86 \times 10^{-5}(km/s)K^{-1}$ and

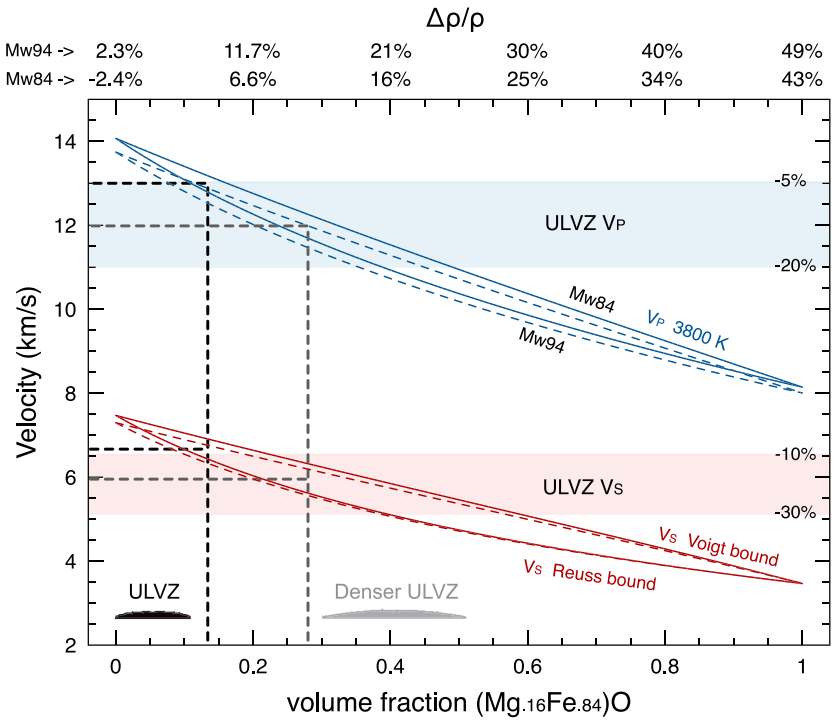

Figure 4. Compressional (V_P, blue) and shear (V_S, red) wave velocities of a mixture of iron-rich magnesiowüstite (Mw) with bridgmanite (Bdg) at 135 GPa and 3800 K. Density anomalies of the Mw84+Bdg model (solid curves) and Mw94+Bdg (dashed curves) are shown on the top axis. Modeled ULVZs with modest or greater velocity drops (lower left corner: $B = 2$ and 6, respectively, for a ULVZ height of 17 km) provide a link between velocity decrement and ULVZ topography.

$\delta V_S/\delta T = -8.57 \times 10^{-5}$(km/s)K^{-1}, calculated by *Wentzcovitch et al.* [2010] for MgO at 135.8 GPa and 3800 K. Density at high temperature was determined using our thermal equation of state [*Wicks et al.*, 2015].

As described by *Bower et al.* [2011], one way to estimate the properties of an iron-rich assemblage at the base of the mantle is to mix iron-rich oxide with bridgmanite, with iron enrichment of the latter determined by partitioning studies. Experimental studies of Fe partitioning between (Mg,Fe)O and bridgmanite find that the distribution coefficient $K_D^{\mathrm{Pv/Mw}} = (X_{\mathrm{Fe}}^{\mathrm{Pv}}/X_{\mathrm{Mg}}^{\mathrm{Pv}})/(X_{\mathrm{Fe}}^{\mathrm{Mw}}/X_{\mathrm{Mg}}^{\mathrm{Mw}})$ decreases as a function of both pressure and iron content—*Auzende et al.* [2008] and *Sakai et al.* [2009] measured from 70 to 100 GPa a drop in K_D from ~0.2 to ~0.07 in iron-poor systems. A phase stability study of the MgO-FeO-SiO_2 ternary measured $K_D^{\mathrm{Pv/Mw}} \sim 0.03$ where $X_{\mathrm{Fe}}^{\mathrm{Mw}} = 0.92$ at 47 GPa [*Tange et al.*, 2009], in addition to observing the same decreasing trend with pressure and composition. While similar studies are needed at core-mantle boundary conditions to clarify trends, we use $K_D^{\mathrm{Pv/Mw}} = 0.03$ here. As a result, X_{Fe} of bridgmanite in equilibrium with Mw84 and Mw94 is 0.14 and 0.32, respectively.

We model the properties of bridgmanite using the finite strain model reported by *Li and Zhang* [2005], replacing initial bulk modulus and its pressure derivative with a more recent study on a suite of iron-bearing bridgmanite samples: $K_{0T} = 264$ GPa, $K'_{0T} = 4$ [*Dorfman et al.*, 2013]. Bulk modulus dependence on Fe content is not resolvable at relatively high iron concentrations [*Dorfman and Duffy*, 2014] and therefore not included, as is shear modulus due to lack of experimental data.

In Figure 4, the Voigt-Reuss mixing envelopes are shown as a function of proportion of oxide with respect to silicate, corrected for natural isotopic abundance of iron. The arithmetic average, called the Voigt-Reuss-Hill average (or simply the Hill average), is often used to approximate the actual state [*Watt et al.*, 1976]. The endpoints for this calculation for Mw84 are $V_P = (14.071, 8.1439$ km/s) and $V_S = (7.4715, 3.4661$ km/s), and for Mw94 are $V_P = (13.744, 8.0049$ km/s) and $V_S = (7.2977, 3.4691$ km/s). Density of a Mw84+Bdg mixture is given by ρ(g/cm^3) $= 2.3784x + 5.5929$, where x = relative fraction of Mw84. Density of a Mw94+Bdg mixture is given by ρ(g/cm^3) $= 2.4122x + 5.9536$, where x = relative fraction of Mw94. The resolution is limited by the uncertainty in the aggregate's state, bounded by uniform strain (Voigt) and stress (Reuss) conditions,

but some general conclusions can be drawn. Addition of modest amounts of iron-rich oxide to iron-enriched bridgmanite can reproduce the range of *P* and *S* wave velocities measured by seismology.

Considering uncertainties, ULVZs with moderate velocity drops are consistent with 10–15% Mw84 mixed with Bdg14 (bridgmanite with 14% Fe per stoichiometric unit) and are consistent with smaller structures with high aspect ratio [*Bower et al.*, 2011]. ULVZs with larger velocity drops are consistent with the presence of 25–30% Mw84 mixed with Bdg14 and are characterized by wider, flatter structures. In these examples, for the same height (17 km), such models would correspond to buoyancy numbers of 2 and 6, respectively [*Bower et al.*, 2011]. Note that a smaller permittable fraction (between 10 and 15%) of Mw94 coexisting with Bdg32 (bridgmanite with 32% Fe per stoichiometric unit) could simultaneously match a range of ULVZ velocity decrements that are associated with similar buoyancy numbers. Adding more Mw94 would yield structures with buoyancy numbers >6 and thus would essentially be flat. One can see how constraining the wave velocities and density permits more constraints on the interpretations and may help rule certain scenarios out.

Using the results presented in this study, a 1-D seismic study now has a way to predict ULVZ shape/lateral extent. Thus, with the assumption that iron-rich (Mg,Fe)O provides a meaningful explanation of many ULVZs, seismic studies that model observations ranging from 1-D to 3-D structures can now constrain the relationship between detailed topography, density, and plausible compositions in these regions.

6. Conclusions

Using data measured in this study, a mineralogical model of ultralow-velocity zones was developed to explore the tradeoff between composition, sound velocity, and ULVZ shape. Not only can dynamically stable ULVZs of reasonable dimensions (width versus height) be created with this model, the density excess required for such long-lived structures are smaller than typically expected (less than 10%). Narrowing the plausible compositions down further would require improved knowledge on the elastic properties of composites (e.g., Voigt and Reuss bounds) and tighter constraints on the temperature-dependent wave velocities. Nevertheless, it can be concluded that simple mixing of magnesiowüstite and iron-enriched bridgmanite can explain the ULVZ velocity decrements and morphology with only modest changes in density.

The nature of the ULVZs potentially holds the key to core-mantle boundary coupling, thus providing insight into the early history of mantle differentiation. If solid and dominated by magnesiowüstite, the increased conductivity [*Fischer et al.*, 2011b; *Ohta et al.*, 2014] would help constrain heat flow across this boundary [*Stix and Roberts*, 1984].

Looking ahead, better knowledge of temperature at the core-mantle boundary is important, as estimates of the CMB temperature fall right around the melting point of very FeO rich assemblages [*Zhang et al.*, 2016]. Iron enrichment has the potential to explain large velocity drops at the base of the mantle, and the consequences of the physical state of this boundary layer on mantle evolution, core-mantle interaction, and magnetic coupling have yet to be fully explored.

Acknowledgments
We thank D.J. Bower and D.V. Helmberger for fruitful discussions. We thank E.E. Alp, T.S. Toellner, and J. Zhao for their assistance at Sector 3; V. Prakapenka at GSECARS; and J. Knight at the ALS. We are thankful to NSF-EAR-CAREER-0956166, NSF-CSEDI-EAR-1161046 for support of this research and to two anonymous reviewers for their thoughtful suggestions. Operations at Sector 3 (APS) and beamline 12.2.2 (ALS) are partially supported by COMPRES. FeO X-ray diffraction measurements were conducted at GSECARS (Sector 13, APS), supported by NSFEAR-1128799 and U.S. DOE, Geosciences (DE-FG02-94ER14466). Use of the APS is supported by the U.S. DOE, Office of Science (DE-AC02-06CH11357) and ALS by the U.S. DOE, Office of Science (DE-AC02-05CH11231). Original data corresponding to those shown in figures and tables are available upon request from the authors.

References

Auzende, A. L., J. Badro, F. J. Ryerson, P. K. Weber, S. J. Fallon, A. Addad, J. Siebert, and G. Fiquet (2008), Element partitioning between magnesium silicate perovskite and ferropericlase: New insights into bulk lower-mantle geochemistry, *Earth Planet. Sci. Lett.*, *269*(1–2), 164–174, doi:10.1016/j.epsl.2008.02.001.

Berryman, J. G. (2000), Seismic velocity decrement ratios for regions of partial melt in the lower mantle, *Geophys. Res. Lett.*, *27*(3), 421–424, doi:10.1029/1999GL008402.

Bower, D. J., J. K. Wicks, M. Gurnis, and J. M. Jackson (2011), A geodynamic and mineral physics model of a solid-state ultralow-velocity zone, *Earth Planet. Sci. Lett.*, *303*, 193–202, doi:10.1016/j.epsl.2006.11.025.

Chen, B., J. M. Jackson, W. Sturhahn, D. Zhang, J. Zhao, J. K. Wicks, and C. A. Murphy (2012), Spin crossover equation of state and sound velocities of $(Mg_{0.65}Fe_{0.35})$ O ferropericlase to 140 GPa, *J. Geophys. Res.*, *117*, B08208, doi:10.1029/2012JB009162.

Cottaar, S., and B. Romanowicz (2012), An unusually large ULVZ at the base of the mantle near Hawaii, *Earth Planet. Sci. Lett.*, *355*, 213–222.

Dorfman, S. M., and T. S. Duffy (2014), Effect of Fe-enrichment on seismic properties of perovskite and post-perovskite in the deep lower mantle, *Geophys. J. Int.*, *197*(2), 910–919.

Dorfman, S. M., Y. Meng, V. B. Prakapenka, and T. S. Duffy (2013), Effects of Fe-enrichment on the equation of state and stability of (Mg, Fe)SiO_3 perovskite, *Earth Planet. Sci. Lett.*, *361*, 249–257.

Dziewonski, A. M., and D. L. Anderson (1981), Preliminary reference Earth model, *Phys. Earth Planet. Inter.*, *25*(4), 297–356, doi:10.1016/0031-9201(81)90046-7.

Fischer, R. A., A. J. Campbell, G. A. Shofner, O. T. Lord, P. Dera, and V. B. Prakapenka (2011a), Equation of state and phase diagram of FeO, *Earth Planet. Sci. Lett.*, *304*, 496–502, doi:10.1016/j.epsl.2011.02.025.

Fischer, R. A., A. J. Campbell, O. T. Lord, G. A. Shofner, P. Dera, and V. B. Prakapenka (2011b), Phase transition and metallization of FeO at high pressures and temperatures, *Geophys. Res. Lett.*, *38*, L24301, doi:10.1029/2011GL049800.

Hammersley, A. O., S. O. Svensson, M. Hanfland, A. N. Fitch, and D. Hausermann (1996), Two-dimensional detector software: From real detector to idealized image or two-theta scan, *High Pressure Res.*, *14*, 235–248, doi:10.1016/j.pepi.2008.07.033.

Helmberger, D., S. Ni, L. Wen, and J. Ritsema (2000), Seismic evidence for ultralow-velocity zones beneath Africa and eastern Atlantic, *J. Geophys. Res.*, *105*(B10), 23,865–23,878.

Helmberger, D. V., L. Wen, and X. Ding (1998), Seismic evidence that the source of the Iceland hotspot lies at the core-mantle boundary, *Nature*, *396*, 251–255.

Hernlund, J., and A. M. Jellinek (2010), Dynamics and structure of a stirred partially molten ultralow-velocity zone, *Earth Planet. Sci. Lett.*, *296*, 1–8, doi:10.1016/j.epsl.2010.04.027.

Hernlund, J., and P. Tackley (2007), Some dynamical consequences of partial melting in Earth's deep mantle, *Phys. Earth Planet. Inter.*, *162*(1–2), 149–163, doi:10.1016/j.pepi.2007.04.005.

Hier-Majumder, S. (2014), Melt redistribution by pulsed compaction within ultralow velocity zones, *Phys. Earth Planet. Inter.*, *229*, 134–143.

Jackson, J. M., E. A. Hamecher, and W. Sturhahn (2009), Nuclear resonant X-ray spectroscopy of (Mg,Fe)SiO_3 orthoenstatites, *Eur. J. Mineral.*, *21*(3), 551, doi:10.1127/0935-1221/2009/0021-1932.

Jacobsen, S. D., H.-J. Reichmann, H. Spetzler, S. J. Mackwell, J. R. Smyth, R. J. Angel, and C. A. McCammon (2002), Structure and elasticity of single-crystal (Mg,Fe)O and a new method of generating shear waves for gigahertz ultrasonic interferometry, *J. Geophys. Res.*, *107*(B2), 2037, doi:10.1029/2001JB000490.

Kato, C., K. Hirose, R. Nomura, M. D. Ballmer, A. Miyake, and Y. Ohishi (2016), Melting in the FeO–SiO_2 system to deep lower-mantle pressures: Implications for subducted Banded Iron Formations, *Earth Planet. Sci. Lett.*, *440*, 56–61.

Knittle, E., and R. Jeanloz (1991), Earth's core-mantle boundary—Results of experiments at high pressures and temperatures, *Science*, *251*(5000), 1438–1443, doi:10.1126/science.251.5000.1438.

Li, B., and J. Zhang (2005), Pressure and temperature dependence of elastic wave velocity of $MgSiO_3$ perovskite and the composition of the lower mantle, *Phys. Earth Planet. Inter.*, *151*(1), 143–154, doi:10.1016/j.pepi.2005.02.004.

Mao, W. L., H. Mao, W. Sturhahn, J. Zhao, V. B. Prakapenka, Y. Meng, J. Shu, Y. Fei, and R. J. Hemley (2006), Iron-rich post-perovskite and the origin of ultralow-velocity zones, *Science*, *312*(5773), 564–565, doi:10.1126/science.1123442.

McCammon, C. A., and L.-g. Liu (1984), The effects of pressure and temperature on nonstoichiometric wüstite, Fe_xO: The iron-rich phase boundary, *Phys. Chem. Miner.*, *10*, 106–113, doi:10.1007/BF00309644.

Nomura, R., K. Hirose, K. Uesugi, Y. Ohishi, A. Tsuchiyama, A. Miyake, and Y. Ueno (2014), Low core-mantle boundary temperature inferred from the solidus of pyrolite, *Science*, *343*(6170), 522–525, doi:10.1126/science.1248186.

Ohta, K., K. Fujino, Y. Kuwayama, T. Kondo, K. Shimizu, and Y. Ohishi (2014), Highly conductive iron-rich (Mg, Fe)O magnesiowüstite and its stability in the Earth's lower mantle, *J. Geophys. Res. Solid Earth*, *119*, 4656–4665, doi:10.1002/2014JB010972.

Pradhan, G. K., G. Fiquet, J. Siebert, A.-L. Auzende, G. Morard, D. Antonangeli, and G. Garbarino (2015), Melting of MORB at core–mantle boundary, *Earth Planet. Sci. Lett.*, *431*, 247–255.

Rost, S., E. J. Garnero, and Q. Williams (2006), Fine-scale ultralow-velocity zone structure from high-frequency seismic array data, *J. Geophys. Res.*, *111*, B09310, doi:10.1029/2005JB004088.

Rost, S., E. J. Garnero, Q. Williams, and M. Manga (2013), Core-mantle boundary landscapes, *Nature*, *6*, 89–90.

Sakai, T., E. Ohtani, H. Terasaki, N. Sawada, Y. Kobayashi, M. Miyahara, M. Nishijima, N. Hirao, Y. Ohishi, and T. Kikegawa (2009), Fe-Mg partitioning between perovskite and ferropericlase in the lower mantle, *Am. Mineral.*, *94*(7), 921–925, doi:10.2138/am.2009.3123.

Shu, J., H.-k. Mao, J. Hu, Y. Fei, and R. J. Hemley (1998), Single-crystal X-ray diffraction of wüstite to 30 GPa hydrostatic pressure, *Neues Jb. Miner. Abh.*, *172*(2–3), 309–323.

Stix, M., and P. Roberts (1984), Time-dependent electromagnetic core-mantle coupling, *Phys. Earth Planet. Inter.*, *36*(1), 49–60.

Struzhkin, V. V., et al. (2001), Nuclear inelastic X-ray scattering of FeO to 48 GPa, *Earth Sci. Rev.*, *110*, 1–25, doi:10.1103/PhysRevLett.87.255501.

Sturhahn, W. (2000), CONUSS and PHOENIX: Evaluation of nuclear resonant scattering data, *Hyperfine Interact.*, *125*(1–4), 149–172, doi:10.1023/A:1012681503686.

Sturhahn, W. (2004), Nuclear resonant spectroscopy, *J. Phys. Condens. Matter*, *16*(5), 497–530, doi:10.1088/0953-8984/16/5/009.

Sturhahn, W., and J. M. Jackson (2007), Geophysical applications of nuclear resonant spectroscopy, *GSA Spec. Pap.*, *421*, 157–174, doi:10.1130/2007.2421(09).

Sun, D., D. V. Helmberger, J. M. Jackson, R. W. Clayton, and D. J. Bower (2013), Rolling hills on the core–mantle boundary, *Earth Planet. Sci. Lett.*, *361*, 333–342, doi:10.1016/j.epsl.2012.10.027.

Tange, Y., E. Takahashi, Y. Nishihara, K.-I. Funakoshi, and N. Sata (2009), Phase relations in the system MgO-FeO-SiO_2 to 50 GPa and 2000°C: An application of experimental techniques using multianvil apparatus with sintered diamond anvils, *J. Geophys. Res.*, *114*, B02214, doi:10.1029/2008JB005891.

Thomas, C. W., and P. D. Asimow (2013), Direct shock compression experiments on premolten forsterite and progress toward a consistent high-pressure equation of state for CaO-MgO-Al_2O_3-SiO_2-FeO liquids, *J. Geophys. Res. Solid Earth*, *118*, 5738–5752, doi:10.1002/jgrb.50374.

Toellner, T. S. (2000), Monochromatization of synchrotron radiation for nuclear resonant scattering experiments, *Hyperfine Interact.*, *125*(1–4), 3–28.

Watt, J. P., G. F. Davies, and R. J. O'Connell (1976), The elastic properties of composite materials, *Rev. Geophys.*, *14*(4), 541–563, doi:10.1029/RG014i004p00541.

Wen, L., and D. V. Helmberger (1998a), A two-dimensional $P-SV$ hybrid method and its application to modeling localized structures near the core-mantle boundary, *J. Geophys. Res.*, *103*(B8), 17,901–17,918, doi:10.1029/98JB01276.

Wen, L., and D. V. Helmberger (1998b), Ultra-low velocity zones near the core-mantle boundary from broadband PKP precursors, *Science*, *279*(5357), 1701–1703, doi:10.1126/science.279.5357.1701.

Wentzcovitch, R. M., Z. Wu, and P. Carrier (2010), First principles quasiharmonic thermoelasticity of mantle minerals, *Rev. Mineral. Geochem.*, *71*(1), 99–128.

Wicks, J. K., J. M. Jackson, and W. Sturhahn (2010), Very low sound velocities in iron-rich (Mg,Fe)O: Implications for the core-mantle boundary region, *Geophys. Res. Lett.*, *37*, L15304, doi:10.1029/2010GL043689.

Wicks, J. K., J. M. Jackson, W. Sturhahn, K. K. Zhuravlev, S. N. Tkachev, and V. B. Prakapenka (2015), Thermal equation of state and stability of $(Mg_{0.06}Fe_{0.94})O$, *Phys. Earth Planet. Inter.*, *249*, 28–42, doi:10.1016/j.pepi.2015.09.003.

Williams, Q., and E. Garnero (1996), Seismic evidence for partial melt at the base of Earth's mantle, *Science*, *273*(5281), 1528–1530, doi:10.1126/science.273.5281.1528.

Wimert, J., and S. Hier-Majumder (2012), A three-dimensional microgeodynamic model of melt geometry in the Earth's deep interior, *J. Geophys. Res.*, *117*, B04203, doi:10.1029/2011JB009012.

Zhang, D., J. M. Jackson, J. Zhao, W. Sturhahn, E. E. Alp, M. Y. Hu, T. S. Toellner, C. A. Murphy, and V. B. Prakapenka (2016), Temperature of Earth's core constrained from melting of Fe and $Fe_{0.9}Ni_{0.1}$ at high pressures, *Earth Planet. Sci. Lett.*, *447*, 72–83, doi:10.1016/j.epsl.2016.04.026.

Zhuravlev, K. K., J. M. Jackson, A. S. Wolf, J. K. Wicks, J. Yan, and S. M. Clark (2010), Isothermal compression behavior of (Mg,Fe)O using neon as a pressure medium, *Phys. Chem. Min.*, *37*, 465–474, doi:10.1007/s00269-009-0347-6.